Electrokinetic effects in nematic suspensions: Single-particle electro-osmosis and interparticle interactions

Article *in* PHYSICAL REVIEW E · August 2018

DOI: 10.1103/PhysRevE.98.022703

CITATION
1

READS
123

7 authors, including:

Oleg M. Tovkach
National Academy of Sciences of Ukraine
18 PUBLICATIONS **95** CITATIONS
SEE PROFILE

Carme Calderer
University of Minnesota Twin Cities
15 PUBLICATIONS **86** CITATIONS
SEE PROFILE

Dmitry Golovaty
University of Akron
71 PUBLICATIONS **369** CITATIONS
SEE PROFILE

Oleg D Lavrentovich
Kent State University
455 PUBLICATIONS **9,986** CITATIONS
SEE PROFILE

Electrokinetic effects in nematic suspensions: Single-particle electro-osmosis and interparticle interactions

Christopher Conklin,[1,*] O. M. Tovkach,[2,3,†] Jorge Viñals,[1,‡] M. Carme Calderer,[4] Dmitry Golovaty,[5] Oleg D. Lavrentovich,[6] and Noel J. Walkington[7]

[1]*School of Physics and Astronomy, University of Minnesota, Minneapolis, Minnesota 55455, USA*
[2]*Department of Mathematics, The University of Akron, Akron, Ohio 44325, USA*
[3]*Bogolyubov Institute for Theoretical Physics, NAS of Ukraine, Metrologichna 14-b, Kyiv 03680, Ukraine*
[4]*School of Mathematics, University of Minnesota, Minneapolis, Minnesota 55455, USA*
[5]*Department of Mathematics, The University of Akron, Akron, Ohio 44325, USA*
[6]*Liquid Crystal Institute, Department of Physics and Chemical Physics Interdisciplinary Program, Kent State University, Kent, Ohio 44242, USA*
[7]*Department of Mathematical Sciences, Carnegie Mellon University, Pittsburgh, Pennsylvania 15213, USA*

(Received 28 December 2017; revised manuscript received 28 June 2018; published 23 August 2018)

Electrokinetic phenomena in a nematic suspension are considered when one or more dielectric particles are suspended in a liquid crystal matrix in its nematic phase. The long-range orientational order of the nematic constitutes a fluid with anisotropic properties. This anisotropy enables charge separation in the bulk under an applied electric field, and leads to streaming flows even when the applied field is oscillatory. In the cases considered, charge separation is seen to result from director field distortions in the matrix that are created by the suspended particles. We use a recently introduced electrokinetic model to study the motion of a single-particle hyperbolic hedgehog pair. We find this motion to be parallel to the defect-particle center axis, independent of field orientation. For a two-particle configuration, we find that the relative force of electrokinetic origin is attractive in the case of particles with perpendicular director anchoring, and repulsive for particles with tangential director anchoring. The study reveals large scale flow properties that are respectively derived from the topology of the configuration alone and from short scale hydrodynamics phenomena in the vicinity of the particle and defect.

DOI: 10.1103/PhysRevE.98.022703

I. INTRODUCTION

The use of applied electric fields to induce fluid motion (electro-osmosis) or suspended particle motion (electrophoresis) is studied when the suspending fluid is a liquid crystal in the nematic phase. The long-range orientational order of the nematic phase defines a fluid with anisotropic properties. Unlike isotropic electrolytes in which charge separation is induced near solid boundaries, the anisotropy of the fluid enables charge separation in the bulk when the nematic director configuration is not uniform. Such a nonuniformity in turn leads to streaming flows that can be manipulated by controlling the molecular orientation of the liquid crystal [1]. A computational study of electro-osmotic flows induced by suspended dielectric particles in a nematic matrix presented in this paper includes the effects of surface anchoring, symmetry of the nematic director field, and dimensionality. Forces on a single particle and interaction forces between two particles are obtained, and compared with experiments.

Microscale manipulation of colloidal particles and fluids by electric fields is a broad area of active scientific research, ranging from fundamental studies of nonequilibrium phenomena [2–5] to the development of practical devices for informational displays, portable diagnostics, sensing, delivery, and cell sorting [6–8]. Electrokinetic fluid transport is important in a variety of engineering, soft matter, and biological systems. For example, electrokinetic flows have been used to create "laboratory on a chip" micropumps, nanofluidic diodes, microfluidic field effect transistors, and *e*-ink devices such as the Amazon Kindle [9–12].

We are primarily interested in suspensions in which the fluid matrix is a *uniaxial nematic liquid crystal*, and the suspended phase is an inert, dielectric particle. A nematic phase consists of rodlike molecules that have no positional order, yet possess long-range orientational order described by a unit nonpolar vector $\boldsymbol{n}$ called a director. Suspended particles distort the long-range orientational order in the matrix, leading to elastic interactions that are absent in normal (isotropic) fluids. In addition, strong anchoring of the liquid crystal at particle surfaces results in topological defects either in the medium or on the surfaces themselves. Such defects, which typically form bound complexes with the suspended particles, are primarily responsible for the unusual transport properties observed in nematic suspensions [1,13].

Our focus is on electrokinetic phenomena, namely, the response of ionic species dissolved in the liquid crystalline matrix to an imposed ac electrostatic field, and the resulting fluid flow and suspended particle motion. Although ionic

*conk0044@umn.edu
†Present address: Department of Physics, University of Massachusetts, Amherst, MA 01003.
‡vinals@umn.edu

impurities are always present in liquid crystal media, their effect has been usually considered as parasitic, and thus to be minimized in applications such as informational displays. On the other hand, the recent discovery of electrokinetic phenomena in nematic suspensions [1,13] has opened a variety of avenues for the creation and control of designer flows that rely on transport induced by coupling to the dissolved ions.

We address here the question of under what conditions the large scale flow induced by a suspended particle can be predicted by topological considerations alone. This would allow simple configurations with their corresponding topological defect charge to be used as building blocks for complex flows engineered for specific applications. As we argue below, whereas some general rules can be advanced, there are important small scale and confinement effects that are important in determining even the qualitative nature of the resulting large scale flows. Confinement affects not only the relative topological stability of nematic defects, but also the structure of hydrodynamic flows. There are only three types of defects possible in our system in three dimensions: line disclinations, point defects (hedgehogs), and point defects that only exist on the surface of the nematic domain (boojums) [14]. In two spatial dimensions, point defects can have integer (hedgehogs) or half-integer (disclinations) degrees. In some configurations, the pair particle defect constitutes an elastic dipole (the hedgehog in the director field), whereas, in others, the elastic configuration is quadrupolar (e.g., the line disclination around the suspended particle, also called a "Saturn ring") [14]. In general, and for reasons of symmetry, dipolar configurations under an imposed uniform field give rise to particle transport, whereas quadrupolar configurations do not [1,15].

Analytic solutions for the director field configuration around a suspended particle are not known, except in the single elastic constant approximation to the nematic free energy, and in two dimensions. In three dimensions, also in the single elastic constant approximation, a variational ansatz has been advanced that reproduces the qualitative features of the director field for a dipolar configuration in an unbounded geometry [16]. More recently, an analytical solution has been obtained for the Saturn Ring configuration, although in the so called tensor order parameter representation [17]. Therefore, numerical computation appears in general necessary to study confined geometries, and the realistic situation in which not all the elastic constants of the nematic are equal. Numerical modeling, however, gives rise to significant mathematical and computational challenges. Two complementary formulations have been advanced depending on whether the order parameter describing the orientation of the nematic is chosen to a unit, apolar, vector field, the director $\hat{\boldsymbol{n}}$, or a symmetric and traceless second order tensor, the tensor order parameter $\boldsymbol{Q}$. The director field is meant to be a macroscopic description of molecular orientation, with a free energy given by the classical Oseen-Frank result [18]. Defects in this description are points, with the elastic energy diverging in the vicinity of the singularity. Instead, the tensor order parameter description is meant to describe nematic order at the mesoscale, and provides a continuous representation of the molecular configuration all through defects, with a finite elastic energy given by the Landau–de Gennes model [19–23]. Both free energies can be mapped into each other, but only for small distortions, i.e., far from singularities. Furthermore, existing computational methods based on the director field representation replace it by a continuous (polar) vector field which cannot represent the original director field in the neighborhood of half-integer degree singularities where it becomes discontinuous. Therefore, this method is restricted to describing integer degree singularities.

These considerations lead to several practical difficulties in the numerical modeling of singular nematic configurations. Either some *ad hoc* regularization scheme is introduced on the director representation (as we do in Sec. II B) (still disallowing half-degree singularities), or the mesoscale tensor order parameter description is used in which the defect region must be explicitly resolved (at a significant computational cost [24]), and with uncertainty about the structure of the phenomenological gradient terms in the free energy, including boundedness issues [19]. To a significant degree, this is one of the central objectives of this paper: To extend our earlier calculations in the tensor order parameter representation for a particle-hedgehog configuration in three dimensions [24], although in an axisymmetric setup, in order to examine the effects of dimensionality and liquid crystal anchoring on charge separation and hydrodynamic flow in configurations that correspond to recent experiments [1,13]. These are prototypical configurations designed to highlight electrokinetic flows induced by a single suspended particle, as well as interactions between two particles, also of electrokinetic origin.

The full Leslie-Ericksen model of the nematic matrix, extended to include electrokinetic phenomena, is described in Sec. II. The director field regularization near singularities that we employ in the numerical analysis is discussed in Sec. II B. Comments given above about possible defect structures are expanded in Sec. II C. We summarize there known results regarding the stability of topological defects as a function of dimensionality and molecular anchoring orientation of the liquid crystal on the surface of the suspended particles. Although the calculations that we present below are two dimensional, the choice of director representation allows us to study a stable hedgehog-particle configuration for the case of homeotropic anchoring. We also examine the case of tangential anchoring in Sec. IV B. In order to do so, we mimic the two boojums that would appear on the surface of the defect in three dimensions by a singular boundary condition on a two-dimensional circle. Following the determination of the spatial charge density, we numerically compute the resulting velocity field. This field is then compared to approximate asymptotic results that we are able to obtain in the Newtonian fluid approximation that reveal the multipolar nature of the velocity field, and its dependence on the type of defect, dimensionality of the system, and anchoring conditions. In particular, we examine a possible resolution of the discrepancy between the flows observed experimentally in a thin film geometry [13], and the results of the axisymmetric numerical analysis of Ref. [24]. Finally, Sec. IV examines interparticle forces induced by electrokinetic phenomena. We show that forces of electrokinetic origin are attractive in the case of homeotropic anchoring, but repulsive for tangential anchoring.

II. MODEL AND CONFIGURATIONS OF INTEREST

The experiments that we wish to model consist of a planar layer of a thermotropic liquid crystal in its nematic phase. The lateral coordinates along the layer are (x, y), and z is the perpendicular direction. The top and bottom cell surfaces at $z = 0$ and h were treated so as to ensure tangential anchoring of the liquid crystal molecules. The focus was on configurations in which the director field of the nematic $\boldsymbol{n} = \hat{\boldsymbol{x}}$ is uniform far from any defects or suspended particles. Spherical dielectric particles were suspended in the fluid, with either homeotropic (perpendicular) or tangential (parallel) anchoring on the surface. The layer is subjected to an external electrostatic field, uniform but oscillatory in time $\boldsymbol{E}_0 = E_0 \cos(\omega t)\hat{\boldsymbol{x}}$. The details of the experimental configuration are described in Ref. [13]. The values of the physical parameters that we use in the numerical computations are generally taken from the experiments in Ref. [1].

A. Governing equations

A liquid crystalline fluid contains $k = 1, \ldots, N$ dissolved ionic species of charge ez_k, where e is the elementary (positive) charge and z_k an integer. The fluid is assumed neutrally charged. The masses of the ionic species molecules are small compared to liquid crystal molecules, and their contribution to the overall mass and momentum densities will be neglected. The number flux of the k species $\boldsymbol{J}_k$ satisfies the conservation law $\partial_t c_k + \nabla \cdot \boldsymbol{J}_k = 0$, where c_k is the concentration of species k. Using standard irreversible thermodynamics for electrolyte solutions [25], we decompose the flux $\boldsymbol{J}_k$ into a reactive component including advection of a local element of volume at the barycentric velocity $\boldsymbol{v}$ (which equals the liquid crystal velocity in our approximation), and a dissipative contribution arising from species diffusion and drift induced by the electrostatic field $\boldsymbol{J}_k = c_k \boldsymbol{v} - \boldsymbol{D} \cdot \nabla c_k + c_k z_k \boldsymbol{\mu} \cdot \boldsymbol{E}$. The quantities $\boldsymbol{D}$ and $\boldsymbol{\mu}$ are the diffusivity and ionic mobility tensors, respectively, which will be assumed to be anisotropic and depend on the local orientation of the liquid crystalline molecule. They are also assumed to obey Einstein's relation $\boldsymbol{D} = \frac{k_B T}{e}\boldsymbol{\mu}$. The equation governing the evolution of the concentration of species k is therefore

$$\frac{\partial c_k}{\partial t} + \nabla \cdot (\boldsymbol{v} c_k) = \nabla \cdot (\boldsymbol{D} \cdot \nabla c_k - c_k z_k \boldsymbol{\mu} \cdot \boldsymbol{E}), \qquad (1)$$

where $\boldsymbol{E}$ is the total electrostatic field. There is no specific information about the dissolved ionic carriers in experiments; only their overall concentration is known. We therefore consider in what follows the case in which only two species of charge $z_1 = 1$ and $z_2 = -1$ are included.

The mobility tensor $\boldsymbol{\mu}$ is assumed to be anisotropic, and dependent on the local orientation of the nematic [26] $\mu_{ij} = \mu_\perp \delta_{ij} + \Delta\mu\, n_i n_j$, where δ_{ij} is the Kroenecker delta. We define $\Delta\mu = \mu_\parallel - \mu_\perp$, where $\mu_\parallel$ and $\mu_\perp$ are the ionic mobilities parallel and perpendicular to $\boldsymbol{n}$, respectively. We focus on the limit of small anisotropy $\Delta\mu/\mu_\perp \ll 1$ ($\Delta\mu/\mu_\perp \approx 0.4$ in Ref. [1]).

In the low frequency range of interest in electrokinetic experiments, the system is assumed to be in electrostatic equilibrium, so that the total electrostatic field in the medium satisfies

$$\epsilon_0 \nabla \cdot (\boldsymbol{\epsilon} \cdot \boldsymbol{E}) = \sum_{k=1}^{N} e z_k c_k. \qquad (2)$$

Although the liquid crystal molecules are not charged, they are polarizable [18]. The nematic is assumed to be a linear dielectric medium, with dielectric tensor $\epsilon_{ij} = \epsilon_\perp \delta_{ij} + \Delta\epsilon\, n_i n_j$, with $\Delta\epsilon = \epsilon_\parallel - \epsilon_\perp$, where $\epsilon_\parallel$ and $\epsilon_\perp$ are the dielectric constants parallel and perpendicular to $\boldsymbol{n}$, respectively. Dielectric anisotropy reinforces or counteracts the effects introduced by mobility anisotropy in electrokinetic flows, leading to novel effects such as flow reversals upon composition or temperature changes of the nematic [27]. For reference, and when feasible, we retain both mobility and dielectric anisotropies in our approximate analytical calculations. However, for simplicity, and because there is no additional qualitative insight to be gained, all the numerical computations reported here correspond to $\Delta\epsilon = 0$.

The liquid crystal is incompressible, $\nabla \cdot \boldsymbol{v} = 0$, and flow is overdamped. Typical velocities are 10 μm/s or smaller, and length scales on the order of microns. Given liquid crystal densities of $\sim 10^3$ kg/m^3 and viscosities ~ 0.1 kg/(ms), one estimates typical Reynolds number Re $\sim 10^{-5}$–10^{-4}. Hence, inertia can be neglected. Momentum balance then reduces to the balance between the incompressible stresses and the body force exerted by the ionic species in a field,

$$\nabla \cdot \boldsymbol{T} + \sum_{k=1}^{N} e z_k c_k \boldsymbol{E} = 0. \qquad (3)$$

The stress tensor is $T_{ij} = -p\delta_{ij} + T^e_{ij} + \tilde{T}_{ij}$, where p is the hydrostatic pressure and $\boldsymbol{T^e}$ is the elastic stress

$$T^e_{ij} = -\frac{\partial f}{\partial(\partial_j n_k)}\frac{\partial n_k}{\partial x_i}, \qquad (4)$$

where f is the Oseen-Frank elastic free energy density. Here, we restrict our analysis to the one elastic constant approximation, namely, $f = (K/2)(\nabla \boldsymbol{n})^2$. In this case, the director field produced by a combination of defects is the linear superposition of the individual director fields, which allows a closer comparison between the numerical results presented below and analytic solutions. General computations and the analysis of differences brought about by considering the full free energy are discussed in Ref. [28]. These differences are of quantitative rather than of qualitative nature.

The viscous stress is given by [18]

$$\begin{aligned}\tilde{T}_{ij} = {} & \alpha_1 n_i n_j n_k n_l A_{kl} + \alpha_2 N_i n_j + \alpha_3 n_i N_j + \alpha_4 A_{ij} \\ & + \alpha_5 n_j A_{ik} n_k + \alpha_6 n_i A_{jk} n_k \end{aligned} \qquad (5)$$

with $N_i = \dot{n}_i - \Omega_{ij} n_j$, and $A_{ij} = \frac{1}{2}(\frac{\partial v_j}{\partial x_i} + \frac{\partial v_i}{\partial x_j})$ and $\Omega_{ij} = \frac{1}{2}(\frac{\partial v_i}{\partial x_j} - \frac{\partial v_j}{\partial x_i})$ the symmetric and antisymmetric parts of the velocity gradient tensor. The coefficients α_i are the Leslie viscosities [29], and $\dot{n}_i = \partial n_i/\partial t + (\boldsymbol{v} \cdot \nabla) n_i$. In some cases below, also for the sake of comparison with analytic asymptotic results, we will restrict our numerical calculations to a Newtonian fluid in which only $\alpha_4 \neq 0$.

Angular momentum conservation defines the dynamics of the director. For overdamped relaxation, a torque balance

yields [18]

$$\boldsymbol{n}\times\boldsymbol{h^0}-\boldsymbol{n}\times\boldsymbol{h}'+\epsilon_0\Delta\epsilon(\boldsymbol{n}\cdot\boldsymbol{E})(\boldsymbol{n}\times\boldsymbol{E})=\boldsymbol{0}, \tag{6}$$

where

$$h_i^0=-\frac{\partial f}{\partial n_i}+\frac{\partial}{\partial x_j}\frac{\partial f}{\partial(\partial_j n_i)}, \qquad h_i'=\gamma_1 N_i+\gamma_2 A_{ij}n_j, \tag{7}$$

where $\gamma_1=\alpha_3-\alpha_2$ and $\gamma_2=\alpha_3+\alpha_2$ are rotational viscosities. The first term in Eq. (6) corresponds to the elastic torque on the director field, the second term corresponds to a viscous torque, and the third term is the torque due to the anisotropy of nematic polarization. This last term is zero in our calculations.

We introduce dimensionless variables as follows. The total concentration of ions is defined as $C=c_1+c_2$, and the charge density as $\rho=e(c_1-c_2)$. We scale spatial variables with particle radius R and time by the inverse frequency of the applied field ω^{-1}. The scale of the charge density is [30] $\epsilon_0\epsilon_\perp E_0/R$, while the total ionic concentration is scaled by its average c_0. The scale of the flow velocity is [30] $\epsilon_0\epsilon_\perp E_0^2R/\alpha_4$, and the pressure scale is $\epsilon_0\epsilon_\perp E_0^2$. The resulting set of dimensionless equations reads as

$$\Omega\frac{\partial C}{\partial t}+W\frac{\partial(Cv_i)}{\partial x_i}=\gamma\frac{\partial}{\partial x_i}\left[\frac{D_{ij}}{D_\perp}\frac{\partial C}{\partial x_j}\right]-Y^2\frac{\partial}{\partial x_i}\left[\rho\frac{\mu_{ij}}{\mu_\perp}E_j\right], \tag{8}$$

$$\Omega\frac{\partial \rho}{\partial t}+W\frac{\partial(\rho v_i)}{\partial x_i}=\gamma\frac{\partial}{\partial x_i}\left[\frac{D_{ij}}{D_\perp}\frac{\partial \rho}{\partial x_j}\right]-\frac{\partial}{\partial x_i}\left[C\frac{\mu_{ij}}{\mu_\perp}E_j\right], \tag{9}$$

$$\frac{\partial}{\partial x_i}\left[\frac{\epsilon_{ij}}{\epsilon_\perp}E_j\right]=\rho, \tag{10}$$

$$\nabla\cdot\boldsymbol{T}+\rho\boldsymbol{E}=0, \qquad \boldsymbol{T}=-p\mathbb{I}+\frac{1}{\mathrm{Er}}\boldsymbol{T}^e+\tilde{\boldsymbol{T}}, \tag{11}$$

$$\boldsymbol{n}\times\boldsymbol{h}^0-\mathrm{Er}\left[\boldsymbol{n}\times\boldsymbol{h}'-\frac{\Delta\epsilon}{\epsilon_\perp}(\boldsymbol{n}\cdot\boldsymbol{E})(\boldsymbol{n}\times\boldsymbol{E})\right]=\boldsymbol{0}, \tag{12}$$

where $\Omega=\omega\tau_\rho$ is the driving frequency relative to the charging time $\tau_\rho=\epsilon_0\epsilon_\perp/(ec_0\mu_\perp)$, $W=\tau_\rho\epsilon_0\epsilon_\perp E_0^2/\alpha_4$, $\gamma=\tau_\rho D_\perp/R^2$, $Y=\epsilon_0\epsilon_\perp E_0/(Rec_0)$, and $\mathrm{Er}=\epsilon_0\epsilon_\perp E_0^2R^2/K$ is the Ericksen number, the ratio of viscous to elastic torques. Note that γ can be also written as $\gamma=\lambda_D^2/R^2$, where $\lambda_D=\sqrt{\epsilon_0\epsilon_\perp k_BT/(e^2c_0)}$ is the Debye length. We also note that in the scaled variables $N_i=(\Omega/W)\partial_t n_i+v_j\partial_j n_i-\Omega_{ij}n_j$. Equations (8)–(12) represent the full set of governing equations in dimensionless form, for only two ionic species, and for overdamped (Stokes) flow. We have also assumed that the electrolyte remains in electrostatic equilibrium at all times.

The numerical computations, as described in Sec. II B, use this complete set of equations with a regularization scheme to address the director field and pressures near singularities [Eqs. (13) and (18)] and are restricted to two spatial dimensions. The electrokinetic experiments that we wish to model are conducted in relatively thin layer configuration with a thickness on the order of 100 μm. However, as discussed in Sec. II C, the thickness h is much greater than R, the suspended particle radius, in order to have a dipolar configuration and systematic flow. Therefore, there needs to be significant three dimensionality in the director field configuration in the immediate vicinity of any suspended particle, as well as three-dimensional flows. Unfortunately, the z component of either one falls below the resolution limit of the experiments, and are unknown at present. It is also possible that, to a degree, the large scale features of charge density and velocity fields are insensitive to these details. Concerning numerical work, earlier research involved a fully three-dimensional, albeit axisymmetric and stationary, configuration [24]. It revealed systematic flows around a suspended particle that were nevertheless reversed relative to the experiments. A full three dimensional, transient numerical analysis of transport in a nematic fluid layer with $h\gg R$, with R in turn much larger that the characteristic defect core size (about 10 nm), is beyond current computational resources. The purpose of this work is then to identify the physical mechanisms determining the long distance dependence of charge density and flow structure induced by simple defect configurations in a layer geometry without undertaking a full numerical computation; hence, we restrict our attention to two dimensions, although we do explore the possible effects of three-dimensional director fields. The approximate analytic results that we use to interpret the numerical results have their own limitations, beyond the fact that analytic solutions to the director field are known only in two dimensions and in the limit of equal elastic constants. We will consider the limits of small mobility anisotropy, low applied field frequency, and will approximate the viscous stress by its Newtonian limit. The relevant approximations are described in detail in the corresponding sections.

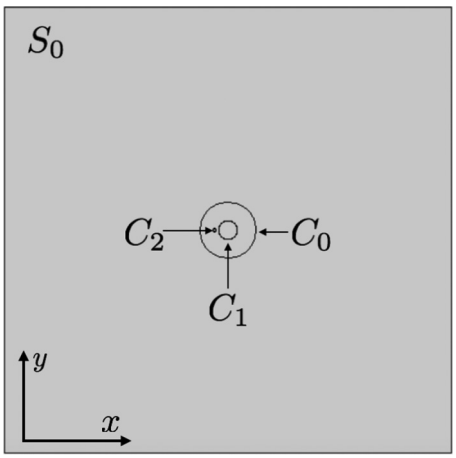

FIG. 1. Computational domain used for single-particle studies. Within a square S_1 is a circular domain C_0 in which the mesh is more finely resolved. C_1 represents the disk-shaped particle, and the mesh is further resolved within the circle C_2 to resolve the topological defect.

B. Computational method

Equations (8)–(12), together with the incompressibility condition, completely describe our model. We solve them numerically in two dimensions with the finite element commercial package COMSOL. Numerical details about mesh generation and code implementation can be found in Refs. [28,30]. Briefly, all numerical solutions are obtained in a square domain S_0 with side length $L=48$, as shown in Fig. 1. We specify the electrostatic potential at the boundaries $\Phi(x=L/2,y)=0$

and $\Phi(x=-L/2,\,y)=-L\cos(t)$, and use Neumann boundary conditions $\partial_y\Phi=0$ at $y=\pm L/2$. Thus, the applied ac field is uniform and parallel to the x axis. The electric potential and the normal component of the dielectric displacement are also continuous across the particle boundary. The experiments on particle transport involve particles with diameter $2R\sim$ 5–50 μm placed in a cell of thickness $h\sim$ 50–100 μm and lateral size $L\sim 10$ mm [13,27,31]. However, the patterned area with nonuniform director field is much smaller, a square of side a few hundred microns, up to a millimeter. Outside this region, the director field is uniform. We do not use open boundary conditions at the edges of the two-dimensional computational cell, but rather we use no-slip conditions in cells of lateral dimension on the order of 100 μm with a fixed and nonuniform director configuration. In addition to no-slip boundary conditions for velocity, we use zero flux boundary conditions for ion currents on all boundaries. We require $\boldsymbol{n}=\hat{\boldsymbol{x}}$ on the boundary of S_0, and $\boldsymbol{n}$ either normal or parallel to the surface of the suspended particle. Within S_0 we create a circle C_0 with radius $r_0=3$; at the center of C_0 is a disk-shaped particle C_1 with radius $r_1=1$. We solve Laplace's equation for Φ within the particle C_1, with $\epsilon_p\partial_r\Phi=\epsilon_\perp\partial_r\Phi$ at $r=1$, where $\epsilon_p=0.1\epsilon_\perp$. A circle C_2 of radius $r_2=0.17$ is located at $(-\sqrt{2},0)$ to resolve the defect that appears due to topological considerations. C_2 consists of 11 808 triangular elements with linear size between 6×10^{-4} and 5×10^{-3}; C_1 has 23 434 triangular elements with linear size between 0.015 and 4.44, C_0 has 43 816 triangular elements with linear size between 11.24×10^{-4} and 0.3, and the rest of the domain has 1990 elements with linear size between 0.015 and 4.44. Additionally, C_0 contains 11 520 quadrilateral elements at the boundary with C_1, and S_0 has 320 quadrilateral elements on the domain boundaries at $x=\pm L/2$ to resolve any charge layers around the electrodes.

For homeotropic anchoring, a hyperbolic hedgehog defect forms in the nematic matrix. The core of the defect is a singularity of the director field. In order to approximate singular director configurations and their energy in the two-dimensional system considered, we replace the normalization constraint $|\boldsymbol{n}|^2=1$ by a free energy term $f_{\rm reg}=K/(4\delta^2)(\boldsymbol{n}^2-1)^2$ which penalizes deviations in the magnitude of $|\boldsymbol{n}|$ from unity. Here, δ is related to the size of the defect core. The elastic free energy is replaced by $f+f_{\rm reg}$, which we just denote by f when considering homeotropic anchoring. The molecular field $\boldsymbol{h^0}$ in this case is

$$h_i^0=K\nabla^2 n_i-\frac{K}{\delta^2}(\boldsymbol{n}^2-1)n_i. \tag{13}$$

Equation (12) and the normalization condition are replaced in the numerical integration with

$$\boldsymbol{h}^0-\mathrm{Er}\left[\boldsymbol{h}'-\frac{\Delta\epsilon}{\epsilon_\perp}(\boldsymbol{n}\cdot\boldsymbol{E})\boldsymbol{E}\right]=\boldsymbol{0}. \tag{14}$$

The inclusion of the regularization does not modify the balance of torques, Eq. (12), since $\boldsymbol{n}\times\boldsymbol{n}=0$.

Since the director is regularized in the numerical solution, there are no director singularities, even though there are defects present. However, since the defect core size is much smaller that the particle radius ($\delta=0.01$ in our numerical computations), we anticipate that the divergence of the elastic stress $\nabla\cdot\boldsymbol{T}^e$ will be replaced by large variations near the defect core that trigger numerical instability. Since the elastic stress is defined as

$$T_{ij}^e=-\frac{\partial f}{\partial(\partial_j n_k)}\frac{\partial n_k}{\partial x_i}, \tag{15}$$

and $f\sim(\nabla\boldsymbol{n})^2$, the divergence of the elastic stress scales as $\boldsymbol{T}^e\sim|\nabla\boldsymbol{n}|^2$. Near defect cores $\nabla\boldsymbol{n}$ scale as r^{-1}; thus, we anticipate near defect cores $\nabla\cdot\boldsymbol{T}^e\sim r^{-3}\sim\delta^{-3}$. We resolve the numerical challenge by noting that the well known elastic equilibrium result $\partial_j T_{ij}^e=-\partial_i f$ can be extended for systems with flow [28]. Using the definition $h_i^0=\partial_j\pi_{ij}-\partial f/\partial n_i$, where $\pi_{ij}=\partial f/\partial(\partial_j n_i)$, one can write the divergence of Eq. (15) as

$$\begin{aligned}-\partial_j T_{ij}^e&=\partial_i n_k\left(h_k^0+\frac{\partial f}{\partial n_k}\right)+\pi_{kj}\partial_j(\partial_i n_k)\\&=h_k^0\partial_i n_k+\frac{\partial f}{\partial n_k}\partial_i n_k+\pi_{kj}\partial_j(\partial_i n_k).\end{aligned} \tag{16}$$

Using Eq. (14), note that $h_k^0\partial_i n_k=\mathrm{Er}[h_k'\partial_i n_k-\frac{\Delta\epsilon}{\epsilon_\perp}(\hat{\boldsymbol{n}}\cdot\boldsymbol{E})E_k\partial_i n_k]$. Using this and the definition of π_{ij}, we can write

$$\begin{aligned}-\partial_j T_{ij}^e&=\frac{\partial f}{\partial n_k}\partial_i n_k+\pi_{kj}\partial_j(\partial_i n_k)\\&\quad+\mathrm{Er}\left[h_k'\partial_i n_k-\frac{\Delta\epsilon}{\epsilon_\perp}(\hat{\boldsymbol{n}}\cdot\boldsymbol{E})E_k\partial_i n_k\right]\\&=\frac{\partial f}{\partial n_k}\partial_i n_k+\frac{\partial f}{\partial(\partial_j n_k)}\partial_j(\partial_i n_k)\\&\quad+\mathrm{Er}\left[h_k'\partial_i n_k-\frac{\Delta\epsilon}{\epsilon_\perp}(\hat{\boldsymbol{n}}\cdot\boldsymbol{E})E_k\partial_i n_k\right].\end{aligned}$$

Then noting $\partial_j(\partial_i n_k)=\partial_i(\partial_j n_k)$ and using the chain rule, we find

$$\partial_j T_{ij}^e=-\partial_i f-\mathrm{Er}\left[h_k'\partial_i n_k-\frac{\Delta\epsilon}{\epsilon_\perp}(\boldsymbol{n}\cdot\boldsymbol{E})E_k\partial_i n_k\right]. \tag{17}$$

The first term on the right-hand side of Eq. (17) diverges as r^{-3} near the defect core. The remaining terms are all linear in $\nabla\boldsymbol{n}$, thus they diverge as r^{-1}. This includes the charge density around a single point defect since $\rho\sim|\nabla\boldsymbol{n}|$. We therefore redefine the pressure as $\tilde{p}=p+f/\mathrm{Er}$ and solve the equation of conservation of momentum numerically for the variable $\tilde{p}$ instead. All terms in the momentum conservation equation then have the same nominal rate of divergence near defect cores, mitigating the numerical difficulties in computing the fluid velocity.

For computational simplicity, we do not directly compute electrophoretic motion of suspended particles, rather we assume they are fixed in space and compute the force on the particle due to both elastic and hydrodynamic stresses $F_i=\int dS_j T_{ij}$. Given the decomposition of the pressure just discussed, the force is separated into an elastic contribution, and a hydrodynamic contribution that includes the effect of

electrokinetic flows

$$F_i = F_i^e + F_i^v = \frac{1}{\mathrm{Er}} \int dS_j \left(f\delta_{ij} + T_{ij}^e \right) + \int dS_j (-\tilde{p}\delta_{ij} + \tilde{T}_{ij}). \quad (18)$$

C. Defect configurations

We investigate flow and particle transport in a nematic fluid governed by the system of equations (8)–(12) and boundary conditions to be specified in which one or two dielectric spherical particles are suspended. The presence of a suspended colloidal particle leads to distortions of the director field due to particle surface anchoring effects. If w is the anchoring energy density, the systems considered are in the limit $K/(wR) \ll 1$, the strong anchoring regime [32]. We focus on two distinct cases, homeotropic anchoring in which $\boldsymbol{n}$ on the surface of the particle is parallel to its normal and tangential anchoring in which $\boldsymbol{n}$ lies on the tangent plane to the particle's surface. For both cases, the director is assumed to be uniform far from the particle $\boldsymbol{n}_0 = \hat{\boldsymbol{x}}$. We consider the topology of this configuration in both two and three dimensions.

1. Two dimensions

In two dimensions, a spherical disk with both homeotropic and tangential anchoring is a topological singularity in the nematic field of charge $(+1)$. Since the assumed far-field boundary condition for the director field is $\boldsymbol{n}_0 = \hat{\boldsymbol{x}}$, the overall topological charge of the system is zero. Therefore, the topological singularity induced by a suspended particle need to be compensated by singularities in the bulk director field. For both homeotropic and tangential anchoring, the two simplest possibilities are either one point defect of charge (-1) or two $(-1/2)$ point defects on either side of the particle. They are both topologically stable, and it is believed that the energy of a configuration with two point defects is lower than that with a single defect [33]. Both configurations are shown in Fig. 2 for both homeotropic and tangential anchoring.

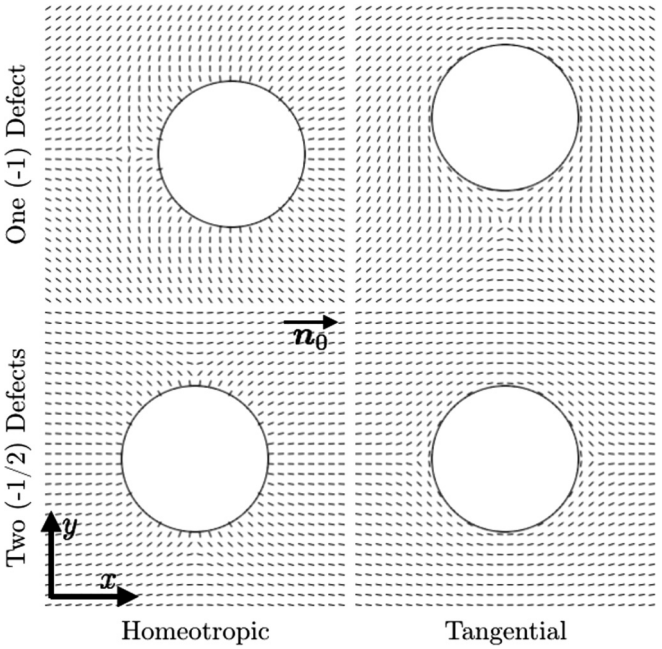

FIG. 2. Possible director fields around a disk in a two-dimensional domain, with far-field director orientation $\boldsymbol{n}_0 = \hat{\boldsymbol{x}}$. For both homeotropic and tangential anchoring, a suspended disk has topological charge $(+1)$, requiring either one (-1) defect or two $(-1/2)$ defects in the bulk.

2. Three dimensions

In three dimensions and homeotropic anchoring, the suspended particle has the same topological charge as a point defect. Just as in two dimensions, the uniform far-field director implies the total topological charge is zero, and thus the suspended particle must induce singularities in the nematic. The two simplest possibilities are a single (-1) point defect [a "hyperbolic hedgehog," Fig. 3] or a $(1/2)$ disclination ring surrounding the particle (a "Saturn ring"), itself equivalent to a point defect of charge (-1). While it is predicted that for small particle radius the Saturn ring configuration has lower elastic energy than the hyperbolic hedgehog [34], only particle-hedgehog configurations observed for larger particle radii are of interest in electrokinetic phenomena. However, confinement also plays a role, such that when the thickness of the layer is not much larger than the radius of the particle, the Saturn ring configuration is again stable [35].

The case of tangential anchoring is more complex: The three-dimensional topological charge of the particle is zero [28]. However, on its two-dimensional surface, given the Poincaré-Brouwer theorem that states that the sum of topological charges be the same as the Euler characteristic of the surface (two for a sphere), there must be surface point defects with charges adding up to two. Such surface defects are known as "boojums." The simplest configuration is one that contains no singularities in the nematic, but two $(+1)$ boojums on the surface of the particle (Fig. 3).

The experiments that motivate our study concern one or more suspended particles in a fluid layer. In the case of homeotropic anchoring, particle radii are a few micrometers (much larger than the $\sim$10 nm typical defect core sizes in a thermotropic liquid crystal), and cell thicknesses are approximately 10 times larger than the particle radius. The defect configuration observed is therefore a hyperbolic hedgehog. Unlike

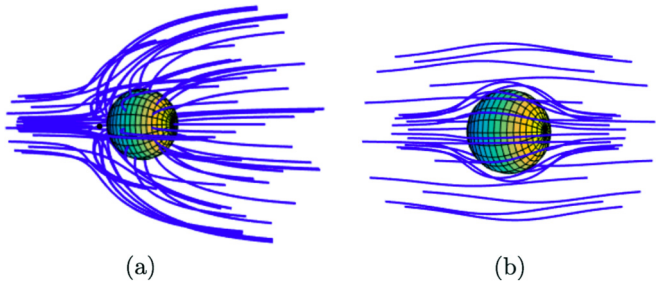

FIG. 3. Three-dimensional director configurations of interest around a spherical particle. With homeotropic anchoring (a), the sphere has the same topological charge as a point defect, and in most experimental systems it induces a hyperbolic hedgehog defect (shown left of the particle). A sphere with tangential anchoring (b) has zero topological charge and requires no defects in the bulk of the nematic, but two boojum defects are required on the particle surface.

a Saturn ring, this configuration breaks reflection symmetry of the suspended particle, and results in its net motion under an applied ac field. In the case of tangential anchoring, particles feature two diametrically opposed boojums which do not lead to net motion. We reiterate, however, that the nematic flows responsible for persistent behavior imaged in experiments appear to be effectively two dimensional at long distances from the particles [13]. Likewise, the director field imaged is also effectively two dimensional, except in the immediate vicinity of the particles where the third component is not resolved.

A computational analysis of three-dimensional electroosmotic flows in the case of a single suspended particle with homeotropic anchoring has been recently given in Ref. [24]. Due to the computational complexity involved, this study was limited to an axisymmetric configuration, constant (dc) electric field, and zero Ericksen number. In order to properly resolve the hyperbolic hedgehog, the director field representation $\boldsymbol{n}$ was replaced by a tensor order parameter $\boldsymbol{Q}$. With this description, the point singularity in $\boldsymbol{n}$ is resolved into a $(-1/2)$ disclination ring of radius small compared with the radius of the particle. Of course, the numerical algorithm must resolve the defect core region, which accounts for the high computational cost of the numerical calculation. Also, the size of the computational cell in [24] is only five times the radius of the particle. Nevertheless, the numerical calculations reveal a stable hyperbolic hedgehog along with the charge distribution induced by the applied field, and the resulting flow in the nematic. Large scale streaming flows are observed, directed from the particle towards the defect near the particle, with the corresponding far-field return flow. The flow is a single, azimuthally symmetric vortex wrapping around the particle. The flow which has been observed experimentally around a single sphere is quite different: it comprises six vortices, and the flow near the defect is toward the particle, the opposite of the numerical computation. It is one of the goals of this study to account for this discrepancy. There are several possibilities to examine. First, the field used in the experiments is oscillatory. Although the frequency is small compared with the other relevant inverse timescales, the structure of the flow induced by either constant or oscillatory body forces is different. Second, the aspect ratio of the computational cell is much smaller than the lateral aspect ratio used in the experiments, therefore possibly constraining the number of vortices that can be formed. Third, the experiments are conducted in a planar cell geometry, not in an axisymmetric cylinder. While the director field, and its topological structure, are clearly three dimensional, the flow field appears to be close to two dimensional, and certainly not axisymmetric.

We therefore report here numerical calculations and some approximate analytic solutions for one or two particles in two spatial dimensions and in configurations in which the lateral dimension is much larger than the particle radius. We also examine the effects of nonzero Ericksen number on interparticle interactions.

III. SINGLE-PARTICLE ELECTROKINETICS

The results reported in this section correspond to $\mathrm{Er} = 0$ so that the director field decouples from the velocity field (for typical experimental values, $\mathrm{Er} \approx 0.04$ [28]). This limit allows the comparison between our numerical results and analytic asymptotic results.

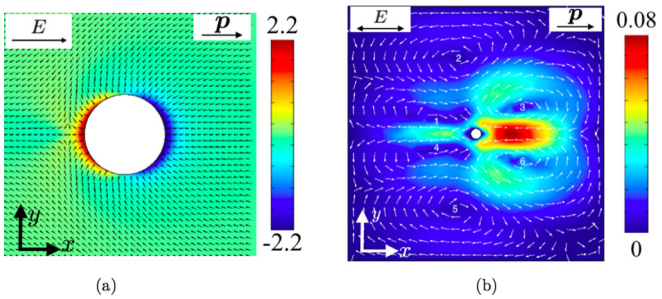

FIG. 4. Subset of the computational domain showing the numerical charge density at $t = 2\pi$ (a), and the time averaged velocity (b) of the electrokinetic flow around a two-dimensional particle with electric field parallel to elastic dipole, plotted in dimensionless units. The flow field comprises six vortices as shown by the labels in the figure. The electrokinetic force on the particle, computed using Eq. (18), is found to point opposite the elastic dipole $\boldsymbol{p}$.

A. Dipolar configuration with homeotropic anchoring

Figure 4 shows our results for a single particle with homeotropic anchoring. The left panel in Fig. 4 shows the instantaneous charge density distribution ρ at $t = \pi/2$ when the field is largest towards the $+x$ direction. Positive and negative charges accumulate around the equators of the particle. Because of the hedgehog, the accumulation on either side is different, leading to a net force on the nematic. Upon reversing the sign of the electric field, the charge distributions are reversed, but the body force remains the same. Hence, streaming flow is induced, which is shown in the right panel in Fig. 4. We have computed the total force on the particle according to Eq. (18), and find that it is negative, i.e., antiparallel to the elastic dipole $\boldsymbol{p}$ shown in Fig. 4 ($\boldsymbol{p}$ directed from the defect to the particle). The direction of this force agrees with the observed particle motion in experiments for the same physical and field parameters.

Returning flows occur due to the boundary conditions on the lateral walls. We observe that the size and shape of the resulting vortices change as we reduce the system size, with only two vortices dominating at $L \sim 10R$ [28]. The experiments of interest are performed with $L \sim 200R$ [13].

Analogous results for the case in which the applied field is perpendicular to $\boldsymbol{p}$ are shown in Fig. 5. Charge accumulation now takes place around the poles, as shown in Fig. 5. The streaming flow, however, is symmetric above and below the particle (along the field direction) but not along the elastic dipole (Fig. 5). The force on the particle computed from Eq. (18) is parallel to $\boldsymbol{p}$, opposite the case of a parallel applied field. Therefore, regardless of the orientation of the applied field, the particle is predicted to move parallel or antiparallel to $\boldsymbol{p}$, not along the direction of the applied field [31,36].

An understanding of the flow field structure, and of differences and similarities with either experiments, or the three-dimensional, axisymmetric numerical results of Ref. [24] can be obtained by examining the case of a Newtonian fluid of viscosity $\eta = \alpha_4$. The large scale structure observed is

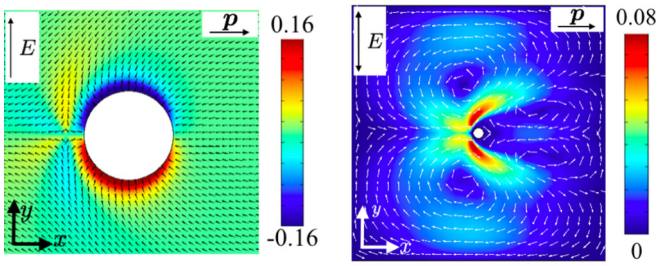

FIG. 5. Numerical charge density at $t = 2\pi$ (a) and time averaged velocity (b) of the induced electrokinetic flow around a two-dimensional particle with electric field perpendicular to elastic dipole, plotted in dimensionless units. We observe four vortices in the flow field, and the electrokinetic force on the particle, computed using Eq. (18), is found to point along the elastic dipole $\boldsymbol{p}$.

qualitatively similar in the general case of the full Oseen-Frank free energy and Leslie viscous tensor, with small quantitative differences such as the distance between the hedgehog and the particle, and the viscous force increasing with decreasing K_1/K_3 [28].

In two dimensions, the charge density far from the particle defect pair can be approximated, to first order in the anisotropies, by [30]

$$\rho(\boldsymbol{r},t) = \left(\frac{\Delta\epsilon}{\epsilon_\perp} - \frac{\Delta\mu}{\mu_\perp}\right)\frac{\cos(t-\delta)}{2\sqrt{1+\Omega^2}} \times \left(\frac{\partial}{\partial x}\cos[2\theta(\boldsymbol{r})] + \frac{\partial}{\partial y}\sin[2\theta(\boldsymbol{r})]\right),$$
$$\tan\delta = \Omega, \tag{19}$$

where the director field has been written as $\hat{\boldsymbol{n}} = (\cos\theta, \sin\theta)$. In two dimensions and in the single elastic constant approximation, there is an analytic solution for the director angle θ, which in the homeotropic anchoring case reads as, on the complex $z = x + iy$ plane,

$$\theta(z) = \mathrm{Im}\left[\log\left(\frac{z^2}{(z+x_0)(z+1/x_0)}\right)\right], \tag{20}$$

which corresponds to a director field with with one (-1) defect at $(-x_0, 0)$ and two image defects within the particle, one of charge $(+2)$ at the origin and one of charge (-1) at $(-1/x_0, 0)$. In elastic equilibrium and in the one constant approximation, $x_0 = \sqrt{2}$. The leading order decay of the corresponding charge density in polar coordinates (r, ϕ) as $r \gg 1$ is

$$\rho(r \gg 1, \phi, t) \approx \left(\frac{\Delta\epsilon}{\epsilon_\perp} - \frac{\Delta\mu}{\mu_\perp}\right)\frac{\cos(t-\delta)}{\sqrt{1+\Omega^2}}\frac{\sqrt{2}\cos(2\phi)}{r^2}, \tag{21}$$

which equals $3/2$ of the long distance charge density induced by a $(-1, +1)$ pair of point defects separated by x_0, whose director angle is given by

$$\theta(z) = \mathrm{Im}\left[\log\left(\frac{z}{z+x_0}\right)\right]. \tag{22}$$

Note both the $(-1, +1)$ pair and the particle defect pair are topologically equivalent yet distinct director fields, with the latter consisting of three singularities (two at $r < 1$).

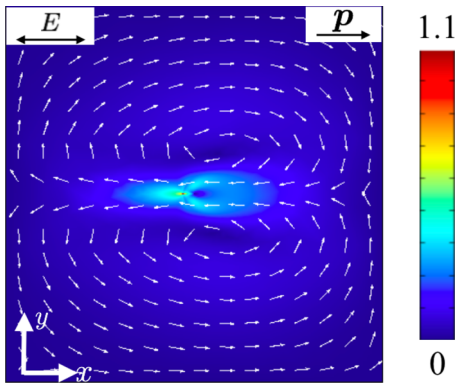

FIG. 6. Numerical velocity field for a $(-1, +1)$ point defect pair, averaged over a period of the applied electric field, plotted in dimensionless units. Note the appearance of only two vortices here in contrast to the six vortices in Fig. 4.

However, the leading order behavior (19) at $r \gg 1$ for either pattern differs by only a factor of $3/2$. Therefore, the far-field dependence of the induced charge follows from the character of the topological dipole, and is independent of short scale details such as considering point defects or a disk of finite radius.

On the other hand, the structure of the large scale flows is sensitive to the details of the defect configuration. Figure 6, for example, shows the velocity field obtained for the point defect pair of Eq. (22). Unlike Fig. 4, the flow comprises only two vortices. In order to understand the difference, we expand the body force, pressure, and velocity fields in a Fourier series in terms of the angular variable

$$\boldsymbol{v}(r,\phi,t) = \sum_n \left(v_n^{(r)}(r,t)e^{in\phi}\hat{\boldsymbol{r}} + v_n^{(\phi)}(r,t)e^{in\phi}\hat{\boldsymbol{\phi}}\right),$$
$$p(r,\phi,t) = \sum_n p_n(r,t)e^{in\phi}, \tag{23}$$

and solve

$$-\nabla p_n + \nabla^2 \boldsymbol{v}_n + \boldsymbol{f}_n = 0, \qquad \nabla\cdot\boldsymbol{v}_n = 0, \tag{24}$$

also decomposing the body force $\boldsymbol{f} = \rho\boldsymbol{E}$ into a Fourier series. From Eq. (21), we find only two nonzero components for $r \gg 1$,

$$\boldsymbol{f}_1 = \left(\frac{\Delta\epsilon}{\epsilon_\perp} - \frac{\Delta\mu}{\mu_\perp}\right)\frac{\cos^2 t}{1+\Omega^2}\frac{\alpha}{2r^2}(\hat{\boldsymbol{r}}\cos\phi + \hat{\boldsymbol{\phi}}\sin\phi), \tag{25}$$
$$\boldsymbol{f}_3 = \left(\frac{\Delta\epsilon}{\epsilon_\perp} - \frac{\Delta\mu}{\mu_\perp}\right)\frac{\cos^2 t}{1+\Omega^2}\frac{\alpha}{2r^2}[\hat{\boldsymbol{r}}\cos(3\phi) - \hat{\boldsymbol{\phi}}\sin(3\phi)], \tag{26}$$

where $\alpha = \sqrt{2}$ for the $(-1, +1)$ point defect pair, and $\alpha = 3/\sqrt{2}$ for the particle-hedgehog pair, due to the difference in director fields. One can then solve for the respective pressures p_n and stream functions ψ_n defined as $\nabla\times(\psi_n\hat{\boldsymbol{z}}) = -\boldsymbol{v}_n$. We find that the stream function harmonic $\psi_1(r,\phi,t)$ does not have a specific far-field dependence; rather, its determination requires the solution of the inner problem near the defects. In

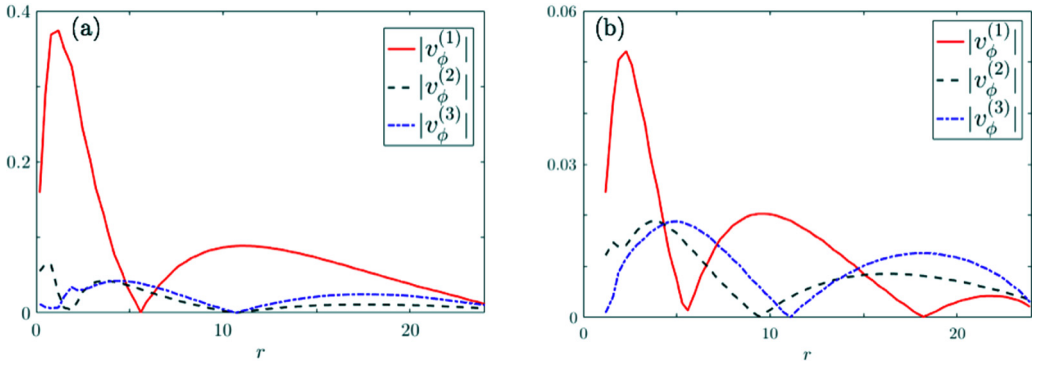

FIG. 7. First three Fourier components of numerical angular velocity for a system with a $(-1, +1)$ point defect set (a) and a particle-defect pair (b), averaged over a period of the field, plotted in dimensionless units as a function of r.

contrast,

$$\psi_3(r,\phi,t) = \psi_{3,in}(r,\phi,t) - \left(\frac{\Delta\epsilon}{\epsilon_\perp} - \frac{\Delta\mu}{\mu_\perp}\right)\frac{\alpha\cos^2 t}{1+\Omega^2}\,\frac{r(r^2-1)^2}{64} \tag{27}$$

has a contribution that needs to be matched to an inner solution $\psi_{3,in}(r,\phi,t)$, but another term, the last term in the right-hand side, which is entirely independent of the inner flow. Therefore, the velocity field always has a projection on the 3ϕ harmonic independent of the inner solution, and a projection along both ϕ and 3ϕ that depend on the flow field near the defect. One would therefore anticipate that a superposition of two or six vortices would be the expected flow field structure corresponding to this dipolar configuration, though this analysis does not preclude the presence of other harmonics due to the solution near the defects.

Figure 7 plots the magnitude of the Fourier components $|v_\phi^{(1)}|$, $|v_\phi^{(2)}|$, $|v_\phi^{(3)}|$ of the angular velocity obtained numerically as a function of r for the director configurations corresponding to a $(-1, +1)$ point defect pair, and the particle-hedgehog configuration. Both cases exhibit a nonzero $|v_\phi^{(3)}|$ term at large r, but $|v_\phi^{(1)}|$ is smaller than $|v_\phi^{(3)}|$ at $r \gtrsim 20$ for the particle defect pair, while for the $(-1, +1)$ point defect set, $|v_\phi^{(1)}|$ is larger than $|v_\phi^{(3)}|$. These results are consistent with the six vortices seen far from the particle in Fig. 4, and the two vortices seen in Fig. 6. This figure also shows that the details of the inner solution lead to a non-negligible $|v_\phi^{(2)}|$ term even in the far field, despite the fact that there is no $e^{2i\phi}$ term in the far-field body force.

B. Effect of dimensionality

Large scale flow structure is sensitive not only to the details of the defect configuration as just shown, but it is also expected to depend on spatial dimensionality. A circular particle in two dimensions corresponds to a cylinder in a thin film rather than a sphere, and the types of defects expected in three dimensions are very different than in two dimensions, as described in Sec. IIC. Furthermore, the leading order behavior of a dipolar field decays as $1/r$ in two dimensions but as $1/r^2$ in three dimensions. Thus, it is possible that some of the basic structure of the large scale flow behavior seen in the experiments in relatively thin films are captured by neither a strictly two-dimensional model as discussed thus far, nor a three-dimensional description in infinite space (an extension of Ref. [24]). Rather, confinement effects in the third dimension may have to be resolved to provide even a qualitative understanding of flows and particle motion. Although we have generally found that the direction of the force of electrokinetic origin on a spatially fixed particle in two dimensions agrees with the observed direction of motion of free particles in a variety of experiments with similar parameter values [27,31,36], surprisingly, the observed electro-osmotic flow around a particle, presented for example in Ref. [13], is qualitatively different than the two-dimensional numerical velocity field shown in Fig. 4. Similarly, charge accumulation is more pronounced on the side of the sphere opposite the hedgehog in the three-dimensional study of Ref. [24], which drives the flow toward the defect. On the other hand, PIV imaging of the experimental cell in Ref. [13] reveals more complex flows, with flow near the defect parallel to the structural dipole. Thus, while a two-dimensional model appears to predict the correct direction of particle motion, it does not appropriately describe the large scale flow.

In order to qualitatively explore possible three-dimensional effects, we consider the approximate solution [16]

$$\boldsymbol{n} = \frac{\boldsymbol{\mathcal{E}}}{|\boldsymbol{\mathcal{E}}|}, \quad \text{with} \quad \boldsymbol{\mathcal{E}}(\boldsymbol{r}) = \hat{\boldsymbol{x}} + \frac{q\boldsymbol{r}}{r^3} + \frac{3x\boldsymbol{r} - r^2\hat{\boldsymbol{x}}}{r^5}, \tag{28}$$

where the value q and the defect position x_0 are determined variationally ($q \approx 3.078$ and $x_0 \approx 1.17$). The leading order decay of Eq. (28) is $1/r^2$, while the two-dimensional equilibrium solution (20) decays only as $1/r$. Since charge density scales with gradients of the director field $\rho \sim \nabla \boldsymbol{n}$, and the viscous force scales with the electrostatic force $\nabla^2 \boldsymbol{v} \sim \rho \boldsymbol{E}$, we expect $\nabla^2 v \sim |\nabla \boldsymbol{n}|$. Therefore, the $1/r^2$ leading order far-field behavior of Eq. (28) implies $\boldsymbol{v} \sim O(r^{-1})$ at $r \gg 1$, while the $1/r$ leading order behavior of the two-dimensional solution implies $\boldsymbol{v} \sim O(\log r)$. Thus, the radial dependency of the velocity field will strongly depend on whether at $r \gg 1$ the decay of the director field is effectively two dimensional or three dimensional.

We have computed the velocity field that follows from the director field of Eq. (28) restricted at $z = 0$, by solving the full hydrodynamic and electrokinetic problems in two dimensions. Figure 8 shows our result for the time averaged velocity field. Unlike both the axisymmetric small cell numerical study, and

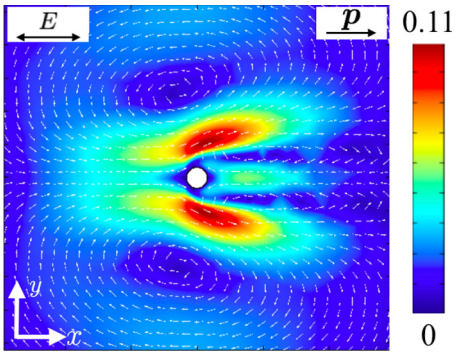

FIG. 8. Two-dimensional average flow field induced by the director field, Eq. (28), at $z = 0$, plotted in dimensionless units.

the fully two-dimensional study in Fig. 4, we find qualitative agreement with the experimental velocity field of Ref. [13]. Specifically, the nematic near the defect flows toward the particle, while the velocity near the right of the particle flows to the left in the figure. Also in agreement with the experiments, we observe two vortices far from the particle that dominate the flow. This is in contrast with the velocity field in Fig. 4 obtained using the two-dimensional equilibrium solution for the director, in which we see flow near the particle always to the left, and six vortices far from the particle.

Such a qualitatively different behavior can be understood by considering the far-field behavior of Eq. (28). For $r \gg 1$,

$$\boldsymbol{n} \approx \hat{\boldsymbol{x}} + \frac{qy}{r^3}\hat{\boldsymbol{y}} = \hat{\boldsymbol{x}} + \frac{q\sin\theta}{r^2}\hat{\boldsymbol{y}}. \tag{29}$$

Using Eqs. (19) and (29), the charge density for $r \gg 1$ to first order in Δ is

$$\rho_{ans}(r,\phi,t) \approx \left(\frac{\Delta\epsilon}{\epsilon_\perp} - \frac{\Delta\mu}{\mu_\perp}\right)\frac{\cos(t-\delta)}{\sqrt{1+\Omega^2}}\frac{q[-1+3\cos(2\phi)]}{r^3}. \tag{30}$$

Comparing Eq. (30) with the far-field charge density generated by the two-dimensional equilibrium director field (21), we see that in addition to a more rapid radial decay, Eq. (30) contains an additional term ρ'_{ans} that is radially symmetric:

$$\rho'_{ans}(r,\phi,t) = -\left(\frac{\Delta\epsilon}{\epsilon_\perp} - \frac{\Delta\mu}{\mu_\perp}\right)\frac{\cos(t-\delta)}{\sqrt{1+\Omega^2}}\frac{q}{r^3}. \tag{31}$$

The body force $\rho'_{ans}\boldsymbol{E}$ due to this extra term written in polar coordinates is

$$\rho'_{ans}\boldsymbol{E} = -\left(\frac{\Delta\epsilon}{\epsilon_\perp} - \frac{\Delta\mu}{\mu_\perp}\right)\frac{\cos(t-\delta)\cos(t)}{\sqrt{1+\Omega^2}}\frac{q}{r^3} \times (\hat{\boldsymbol{r}}\cos\phi - \hat{\boldsymbol{\phi}}\sin\phi). \tag{32}$$

Thus, the radial term leads to an additional term in the body force with dipolar symmetry. Furthermore, under the assumption of Newtonian stress, the part of Eq. (32) that does not average to zero generates a velocity field with stream function

$$\psi'(r,\phi,t) = \psi'_{in}(r,\phi,t) + \left(\frac{\Delta\epsilon}{\epsilon_\perp} - \frac{\Delta\mu}{\mu_\perp}\right)\frac{\cos^2 t}{1+\Omega^2}\sin\phi. \tag{33}$$

Thus, unlike the solution for a strict two-dimensional director, the presence of the additional radial term in the charge density produces a dipolar far-field term in the stream function which is independent of the inner solution. While one must determine the charge and velocity field near the particle in order to fully compute the velocity field, the presence of this dipolar term in the stream function is consistent with the numerical and experimental observation of two vortices dominating the flow behavior at $r \gg 1$.

IV. INTERPARTICLE INTERACTIONS

We turn next to investigating electrokinetic induced interactions between two suspended particles. Studies of elastic interactions between multiple colloidal particles in a nematic suspension have been performed experimentally [16,37], analytically [33,38–42], and numerically [43–46], but there are no studies addressing the effect of electrokinetics on interparticle interactions. Knowledge of interparticle interactions is necessary, for example, to interpret observed clustering and swarming effects [15]. In the calculations that follow we allow $\mathrm{Er} \neq 0$, and hence the director field is computed simultaneously with the velocity field.

A. Homeotropic anchoring

We consider two circular particles in two dimensions with homeotropic anchoring, each with a companion hedgehog defect, and we compute the forces on the suspended particles. The total force on each particle is computed by integrating the normal component of the stress over the particle surface, as given in Eq. (18). In elastic equilibrium without flow, particle-defect pairs align [16,46,47]. Since electrokinetic forces on a single particle are along the elastic dipole $\boldsymbol{p}$, we expect that when subject to an electric field, and thus a nonzero hydrodynamic force, particle pairs will remain collinear, with a net force along $\pm\boldsymbol{p}$, although the interparticle separation may change. There are a number of numerical challenges to solving the full system of equations with moving particles (among them, dynamical remeshing); instead, we investigate the electrokinetic effect on the average separation of two collinear particles by finding the separation length at which the time averaged difference in hydrodynamic force balances the difference in elastic force. Under these conditions, the pair would move with a common velocity while oscillating about this new separation length.

Figure 9 shows our numerical results for the director field at $t = 2\pi$, the corresponding instantaneous charge density, and the time averaged velocity field for two particles at separation $s = 0.426$ (s is the shortest distance between the particles surfaces). Far from the two particles, we anticipate the director to have a dipolar structure, leading to six vortices. Fluid motion between the two particles is complex, but it appears that when the electric field points to the right, as in Fig. 9, the left particle screens positive charges moving right, and the right particle screens negative charges moving left, leading to smaller charge accumulation between the particles than if they were alone.

The force on either particle is computed by integrating the normal component of the stress tensor along the particle surface $\boldsymbol{F} = \oint \boldsymbol{T}\cdot\boldsymbol{\nu}\,dS$. It is useful to separate $\boldsymbol{F}$ into a component

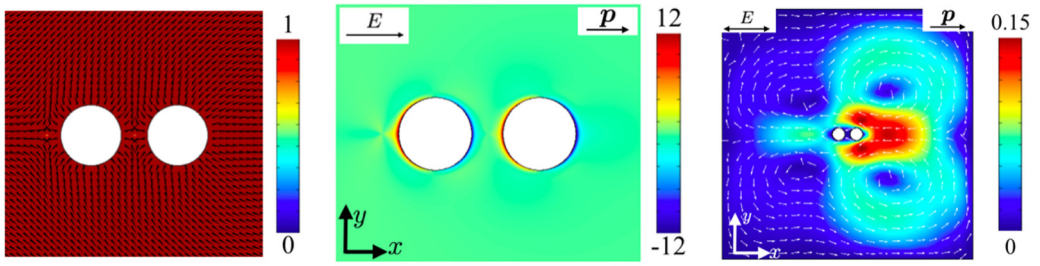

FIG. 9. Results for two particles with homeotropic anchoring, separated by $s = 0.426$, plotted in dimensionless units. (a) Director field at $t = 2\pi$, with magnitude plotted in color. (b) Charge density at $t = 2\pi$, with electric field pointing to the right. (c) Velocity field averaged over a period of the applied field.

$\boldsymbol{F}^e$ originating from elastic distortions, and a component $\boldsymbol{F}^v$ originating from hydrodynamic flow. As noted in Sec. II B, the divergence of the elastic stress $\boldsymbol{T}^e$ leads to a contribution $-f/\mathrm{Er}$ in the pressure, where f is the elastic free energy, and we define $\tilde{p} = p + f/\mathrm{Er}$ as the pressure contribution due to nematic flow. Grouping the elastic contributions together, the force $\boldsymbol{F}^e$ on a particle due to elastic distortions is

$$F_i^e = \frac{1}{\mathrm{Er}} \oint \left(f\delta_{ij} + T_{ij}^e \right) \nu_j dS, \tag{34}$$

where $\boldsymbol{\nu}$ is the unit normal to the particle. The force $\boldsymbol{F}^v$ on the particle due to hydrodynamic flow is the integral of the remaining terms

$$F_i^v = \oint (-\tilde{p}\delta_{ij} + \tilde{T}_{ij}) \nu_j dS. \tag{35}$$

Figure 10 plots the difference in elastic and time averaged hydrodynamic force between two particles as a function of particle separation at $\mathrm{Er} = 2$. The equilibrium configuration of the translating pair would correspond to the zero of the interparticle force. For the range of parameters investigated, the first term on the right-hand side of Eq. (35) produces a leftward force on the right particle and a rightward force on the left particle. The second term on the right-hand side of Eq. (35) produces a leftward force on both particles but with a larger magnitude for the right particle. Summing both terms together, the total hydrodynamic force on both particles is to the left, but is larger for the right particle than for the left. Therefore, hydrodynamic forces not only drive motion of the center of mass of the two particles, but also lead to an effective interparticle attraction that is nearly independent of separation s, as seen by the negative force difference in Fig. 10. On the other hand, the elastic force difference is repulsive at short distances and becomes attractive as s increases. We find the total average force difference is zero at $s \approx 0.429$, a smaller separation than the elastic energy alone would predict. Thus, while the total force on the two particles is not zero (the dipolar nature of the director field causes their center of mass to translate), the relative separation of the two particles is smaller than in the absence of the electrostatic field.

We finally show our results for the predicted separation as a function of the Ericksen number. Since electrokinetic flow produces an attractive hydrodynamic force, we anticipate the

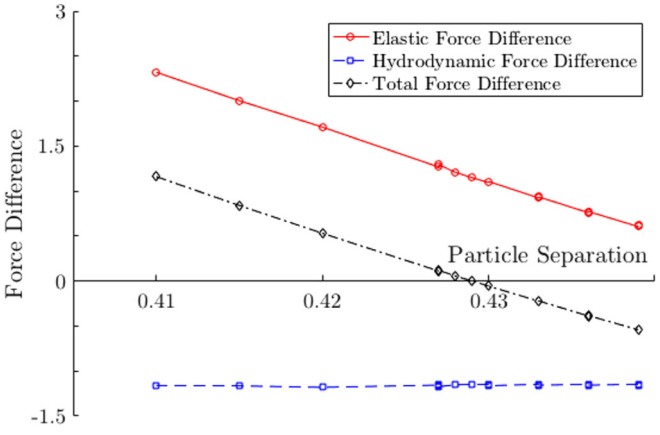

FIG. 10. Numerically computed difference in hydrodynamic and elastic force between two particles with homeotropic anchoring at $\mathrm{Er} = 2$, averaged over a period of the field and plotted as a function of particle separation in dimensionless units. For the range of parameters plotted, the hydrodynamic forces always result in particle attraction, while the elastic forces are more repulsive at closer distances. The total force difference is also plotted, and we see the equilibrium position occurs at $s \approx 0.429$.

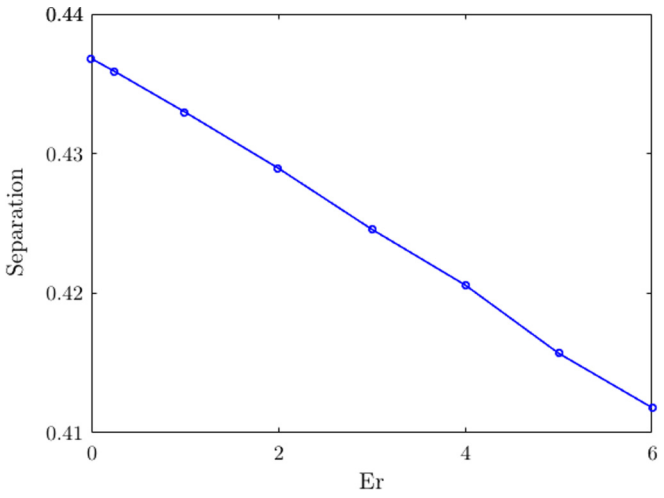

FIG. 11. Particle separation in dimensionless units as a function of Ericksen number. The decrease in separation as Er increases implies the hydrodynamic electrokinetic force is attractive.

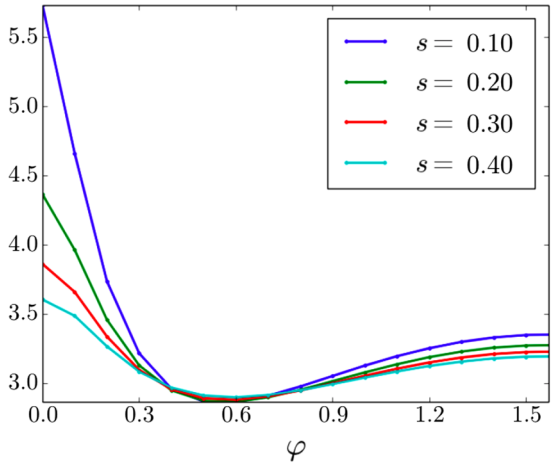

FIG. 12. Elastic energy (dimensionless units) for a system of two circular particles with tangential anchoring at various surface to surface separations s, and relative orientations φ (rad).

average particle separation will decrease as a the relative size of the hydrodynamic force increases. Figure 11 shows the stable separation distance as a function of Ericksen number. The separation decreases as the Ericksen number increases, consistent with an attractive electrokinetic force. Note that Fig. 11 plots only the average particle separation. Since the electric field is oscillatory, the hydrodynamic force and therefore the interparticle separation will also oscillate. We have not considered the limit in which the amplitude of particle oscillations becomes on the order of the interparticle separation.

B. Tangential anchoring

Spherical particles with tangential anchoring also form chains in elastic equilibrium and in the absence of any electrokinetic effects. However, the chains are oriented at an angle of $\sim 30^\circ$ relative to the far-field director [37]. As discussed in Sec. II C, there are no singularities in the bulk nematic, just two surface singularities of charge $(+1)$ on the particle's surface ("boojums"). In two dimensions, the configuration of minimum energy comprises two $(-1/2)$ point defects on either side of the particle. In order to mimic the tangential anchoring case with a numerical method constrained to a polar representation of $\boldsymbol{n}$ and in two dimensions, we specify the following director angle $\theta = \tan^{-1}(-\nu_x/\nu_y)$ on the particle surface where $\boldsymbol{\nu}$ is its unit normal. This boundary condition leads to two defects at opposite ends of each particle which are one-dimensional analogs of boojums on a sphere. An additional advantage of this choice (with no singularities in the bulk nematic) is that the finite element method can handle singularities on boundaries, hence, there is no need for a regularization of the director field.

We have first confirmed that in the absence of electrokinetic effects the configuration of two circular particles that minimizes the elastic free energy forms an angle with the far-field director. Figure 12 shows the computed energy at a variety of separations and angles. We find the minimum of the elastic energy at $\varphi \approx 31.5^\circ$, consistent with the experimental results in Ref. [37]. We also find the energy is minimized when the separation between the particle surfaces is approximately $s \approx 0.2$.

Figure 13 shows the instantaneous charge density distribution for two circular particles located at a separation and angle for which they would be in elastic equilibrium in the absence of electrokinetic flow, along with the corresponding average velocity. Unlike the case of homeotropic anchoring, we observe large velocity variations between the two particles. Since this configuration does not have a dipole moment, we do not expect any systematic flow, and indeed we find no net force on the two particle system. However, we do find the two particles experience a repulsive hydrodynamic force and positive torque about their center of mass, suggesting that if free to move the particle separation would increase, as would their orientation angle relative to no electrokinetic flow. Hence, and in contrast with the case of homeotropic anchoring, electrokinetic effects lead to repulsion in the case of tangential anchoring.

V. DISCUSSION AND CONCLUSIONS

We have presented a comprehensive study of the electrokinetic flows that are induced by dielectric spherical particles suspended in a liquid crystal matrix which is in the nematic phase. Particular liquid crystal anchoring conditions on the particle surface result in topological defects in the nematic matrix. The resulting director distortion leads to ionic charge separation in the bulk matrix under an applied field, and to streaming flows.

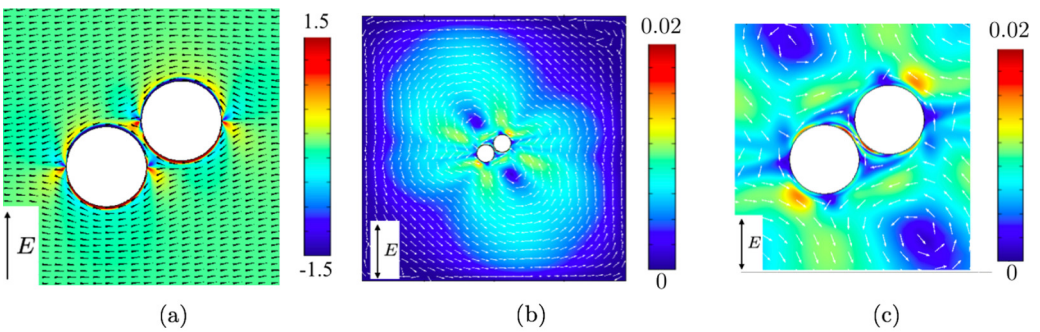

FIG. 13. (a) Instantaneous charge density corresponding to two circular particles fixed at the separation and angle that minimize the elastic free energy. The oscillatory electric field point in the y direction. (b) Time averaged electrokinetic velocity, which is shown magnified in (c) to highlight the appearance of boundary layer flows near particle surfaces. All values are in dimensionless units.

For a single particle and homeotropic anchoring, we have studied a dipolar configuration comprising the spherical particle and an accompanying hyperbolic hedgehog. We find that the asymmetry in charge separation between the side of the sphere near the hedgehog and the opposing side leads to a net force on the particle which is directed from the particle towards the defect when the applied field is parallel to the elastic dipole, and in the opposite direction for the transverse case. This is in agreement with experiments showing net translation of the pair particle defect towards the defect under a parallel oscillatory field, and away from the defect under a transverse applied field. Whereas the far-field charge density follows from the dipolar nature of the configuration, the far-field velocity is more complex. We numerically observe two, four, or six vortices, depending on the applied field and the far-field director, and on the relative contribution between angular harmonics determined by the inner solution of the hydrodynamic problem. We show that the far-field velocity obtained in two dimensions is qualitatively different from the experiments, and from an earlier three-dimensional solution in an axisymmetric geometry and under steady (dc) applied field. We have analyzed the discrepancy and traced it to the competition between a three-dimensional director field in the thin film geometry of the experiments, and effectively two-dimensional flows.

We also studied two particles suspended in the nematic matrix and obtained the interaction force between the particles of electrokinetic origin. Homeotropic anchoring leads to an attractive force between the particles, which we interpret as due to charge separation screening between the two particles. The effect scales with the Ericksen number. For tangential anchoring, the interaction is repulsive. The axis joining the centers of the particle pair is seen to rotate relative to the far-field nematic, and the applied electrostatic field originates significant flows between the two particles, a flow that is absent in the homeotropic case. We have also shown in the homeotropic case that the force on the particle is along the line joining the particle and the defect, irrespective of the orientation of the applied electric field.

Our study has a significant number of limitations. First and foremost, due to the computational complexity of the problem, our results are restricted to a two-dimensional system. In addition, we have considered a representation of the director field as a polar vector, a fact that artificially precludes half-integer singularities. A hedgehog is then stable as an accompanying defect to the immersed particle in two dimensions, a configuration that is only stable in three dimensions when the particle dimensions are two or three orders of magnitude larger than the defect core scale, but small compared with the thickness of the sample. Such a configuration is difficult to study computationally. Nevertheless, we are able to argue how the large scale structure of the induced flow observed in the experiments is likely due to three-dimensional effects in the director field. A complete elucidation of the electrophoretic flows observed experimentally will require a solution that can incorporate thin film crossover phenomena in both director and velocity fields.

In addition to the two-dimensional approximation, the lateral dimensions of the experimental cell can be from about 40 to about 200 times the particle radius [13], while the numerical results were performed with $L = 48R$. We have observed qualitative differences in flow structure in small cells (when $L \sim 10R$ [28]), due to the no-slip boundary conditions on the cell walls. Thus, it is possible that increasing the size of the computational domain could result in changes in the flow structure. However, confinement effects induced by our computational domain relative to the experimental cell are not likely a significant concern because the numerically determined velocity Fourier components agree with the infinite space limit of $L \gg R$. Of course, the structure of the flow in Fig. 8 agrees with the experiments [13].

Despite these shortcomings, comparison between our results and experiment, and with topology based arguments in the one constant approximation and Newtonian flow, has helped identify general features of charge separation induced by nematic order and mobility anisotropy depending on the structure of the particle-defect pair, the force induced on a single particle, and the interaction force between a pair of particles. General arguments can be given to predict some global features of the large scale flows of electrokinetic origin, although a detailed prediction still requires the solution of the hydrodynamic problem in the vicinity of the defects.

ACKNOWLEDGMENTS

This research has been supported by the National Science Foundation under Contract No. DMS 1435372, by the Minnesota Supercomputing Institute, and by the Extreme Science and Engineering Discovery Environment (XSEDE) [48], which is supported by National Science Foundation Grant No. ACI 1548562. O.D.L. acknowledges the support of NSF Grant No. DMR-1507637.

[1] C. Peng, Y. Guo, C. Conklin, J. Viñal, S. V. Shiyanovskii, Q.-H. Wei, and O. D. Lavrentovich, Phys. Rev. E **92**, 052502 (2015).
[2] M. Z. Bazant, M. S. Kilic, B. D. Storey, and A. Ajdari, Adv. Colloid Interface Sci. **152**, 48 (2009).
[3] I. Aranson, Phys. Usp. **56**, 79 (2013).
[4] A. Zöttl and H. Stark, J. Phys.: Condens. Matter **28**, 253001 (2016).
[5] O. D. Lavrentovich, Curr. Opin. Colloid Interface Sci. **21**, 97 (2016).
[6] J. Dobnikar, A. Snezhko, and A. Yethiraj, Soft Matter **9**, 3693 (2013).
[7] A. Ramos, *Electrokinetics and Electrohydrodynamics in Microsystems* (Springer, Wien, 2011).
[8] M. Bazant and T. Squires, Curr. Opin. Colloid Interface Sci. **15**, 203 (2010).
[9] V. Studer, A. Pépin, Y. Chen, and A. Ajdari, The Analyst **129**, 944 (2004).
[10] C. Zhao and C. Yang, Microfluid Nanofluid **13**, 179 (2012).
[11] B. Comiskey, J. D. Albert, H. Yoshizawa, and J. Jacobson, Nature (London) **394**, 253 (1998).
[12] S. Klein, Liq. Cryst. Rev. **1**, 52 (2013).

[13] I. Lazo, C. Peng, J. Xiang, S. Shiyanovskii, and O. Lavrentovich, Nat. Commun. **5**, 5033 (2014).
[14] H. Stark, Phys. Rep. **351**, 387 (2001).
[15] S. Hernández Navarro, P. Tierno, J. Farrera, J. Ignés Mullol, and F. Sagués, Angewandte Chemie-International Edition **53**, 10696 (2014).
[16] P. Poulin, H. Stark, T. Lubensky, and D. Weitz, Science **275**, 1770 (1997).
[17] S. Alama, L. Bronsard, and X. Lamy, Phys. Rev. E **93**, 012705 (2016).
[18] P. de Genne and J. Prost, *The Physics of Liquid Crystals* (Clarendon Press, Oxford, 1993).
[19] P. Bauman and D. Phillips, Calc. Variations Partial Differential Equations **55**, 81 (2016).
[20] J. M. Ball and A. Majumdar, Mol. Cryst. Liq. Cryst. **525**, 1 (2010).
[21] J. M. Ball and A. Zarnescu, Arch. Ration. Mech. Anal. **202**, 493 (2011).
[22] R. Ignat, L. Nguyen, V. Slastikov, and A. Zarnescu, Arch. Ration. Mech. Anal. **215**, 633 (2015).
[23] A. Majumdar and A. Zarnescu, Arch. Ration. Mech. Anal. **196**, 227 (2010).
[24] O. M. Tovkach, C. Conklin, M. C. Calderer, D. Golovaty, O. D. Lavrentovich, J. Viñals, and N. J. Walkington, Phys. Rev. Fluids **2**, 053302 (2017).
[25] S. de Groot and P. Mazur, *Non-equilibrium Thermodynamics* (Dover, New York, 1984).
[26] W. Helfrich, J. Chem. Phys. **51**, 4092 (1969).
[27] S. Paladugu, C. Conklin, J. Viñals, and O. D. Lavrentovich, Phys. Rev. Appl. **7**, 034033 (2017).
[28] C. Conklin, Electrokinetic Phenomena and Singularity-Driven Flows in Nematic Liquid Crystals, Ph.D. thesis, University of Minnesota, 2017.
[29] I. Stewart, *The Static and Dynamic Continuum Theory of Liquid Crystals* (Taylor and Francis, New York, 2004).
[30] C. Conklin and J. Viñals, Soft Matter **13**, 725 (2017).
[31] O. Lavrentovich, I. Lazo, and O. Pishnyak, Nature (London) **467**, 947 (2010).
[32] O. Lavrentovich, Soft Matter **10**, 1264 (2014).
[33] M. Tasinkevych, N. M. Silvestre, P. Patrício, and M. M. Telo da Gama, Eur. Phys. J. E **9**, 341 (2002).
[34] H. Stark, Eur. Phys. J. B **10**, 311 (1999).
[35] Y. Gu and N. L. Abbott, Phys. Rev. Lett. **85**, 4719 (2000).
[36] I. Lazo and O. D. Lavrentovich, Philos. Trans. R. Soc. London A **371**, 20120255 (2013).
[37] I. I. Smalyukh, O. D. Lavrentovich, A. N. Kuzmin, A. V. Kachynski, and P. N. Prasad, Phys. Rev. Lett. **95**, 157801 (2005).
[38] R. W. Ruhwandl and E. M. Terentjev, Phys. Rev. E **55**, 2958 (1997).
[39] T. C. Lubensky, D. Pettey, N. Currier, and H. Stark, Phys. Rev. E **57**, 610 (1998).
[40] V. M. Pergamenshchik and V. A. Uzunova, Phys. Rev. E **83**, 021701 (2011).
[41] D. Pettey, T. C. Lubensky, and D. R. Link, Liq. Cryst. **25**, 579 (2010).
[42] O. M. Tovkach, S. B. Chernyshuk, and B. I. Lev, Phys. Rev. E **86**, 061703 (2012).
[43] F. R. Hung, O. Guzmán, B. T. Gettelfinger, N. L. Abbott, and J. J. de Pablo, Phys. Rev. E **74**, 011711 (2006).
[44] K. Tojo, A. Furukawa, T. Araki, and A. Onuki, Eur. Phys. J. E **30**, 55 (2009).
[45] T. Kishita, N. Kondo, K. Takahashi, M. Ichikawa, J. I. Fukuda, and Y. Kimura, Phys. Rev. E **84**, 021704 (2011).
[46] J. I. Fukuda, H. Stark, M. Yoneya, and H. Yokoyama, Phys. Rev. E **69**, 041706 (2004).
[47] V. M. Pergamenshchik, Eur. Phys. J. E **37**, 1 (2014).
[48] J. Towns, T. Cockerill, M. Dahan, I. Foster, K. Gaither, A. Grimshaw, V. Hazlewood, S. Lathrop, D. Lifka, G. D. Peterson, R. Roskies, J. R. Scott, and N. Wilkins-Diehr, Comput. Sci. Eng. **16**, 62 (2014).